The Mid-Infrared Instrument for JWST VI: The Medium Resolution Spectrometer

Wells, Martyn[1], Glasse, A. C. H.[1], Azzollini, Ruymán[2], Brandl, B. R.[3], Fischer, Sebastian[4], Geers V. C.[2], Glauser, A. M.[5], Hastings, Peter[1], Jager, Rieks[6], Kroes, Gabby[6], Justtanont, K.[7], Lahuis, Fred[8], Lee, David[1], Martinez-Delgado, I.[9], Martinez-Galarza, J. R.[10], Meijers, M.[6], Morrison, J.[15], Nakos, Theodoros[11], Oudenhuysen, Ad[6], Parr-Burman, P.[1], Pel, J.-W.[6], Vandenbussche, Bart[12], Venema, Lars[6], Visser, Huib[13], Wright, David[14], Wright, G. S.[1]

ABSTRACT. We describe the design and performance of the Medium Resolution Spectrometer (MRS) for the JWST-MIRI instrument. The MRS incorporates four coaxial spectral channels in a compact opto-mechanical layout that generates spectral images over fields of view up to 7 x 7 arcseconds in extent and at spectral resolving powers ranging from 2,500 to 3,700. Each channel includes an all-reflective integral field unit (IFU): an 'image slicer' that reformats the input field for presentation to a grating spectrometer. Two 1024 x 1024 focal plane arrays record the output spectral images with an instantaneous spectral coverage of approximately one third of each channel's full wavelength range. The full 5 to 28.5 μm spectrum is then obtained by making three exposures using gratings and pass-band selecting filters that are selected using just two three-position mechanisms. The expected on-orbit optical performance is presented, based on testing of the MIRI Flight Model, and including spectral and spatial coverage and resolution. The point spread function of the reconstructed images is shown to be diffraction limited and the optical transmission is shown to be consistent with the design expectations.

1 INTRODUCTION

The MIRI Medium Resolution Spectrometer (MRS) is an Integral Field Unit (IFU) spectrometer that covers the wavelength range from 5 to 28.5 μm at spectral resolving powers of ~3000. It consists of 4 channels that have co-aligned fields of view, simultaneously observing the wavelength ranges listed in Table 1 with individually optimised IFUs, collimators and gratings.

Section 2 of this paper provides a description of the optical design, including the rationale for choosing the IFU concept and its impact on how observations are carried out. Section 3 then describes the expected on-orbit optical performance of the MRS as measured during cryogenic testing, and with a description of the procedure used to construct calibrated spectral data cubes from the raw measured images. The impact of particular features of the MRS, including spectral fringing and straylight are also discussed here.

[1]The UK Astronomy Technology Centre, Blackford Hill, Edinburgh, EH9 3HJ, UK.
[2]Dublin Institute for Advanced Studies, Astronomy and Astrophysics Section, 31 Fitzwilliam Place Dublin 2 Ireland.
[3]Leiden Observatory, Leiden University, PO Box 9513, 2300 RA, Leiden, The Netherlands.
[4]Deutsches Zentrum für Luft- und Raumfahrt (DLR), Königswinterer Str. 522-524, 53227 Bonn, Germany
I. Physikalisches Institut, Universität zu Köln, Zülpicher Str. 77, 50937 Köln, Germany
[5]ETH, Rämistrasse 101, 8092 Zurich, Switzerland.
[6]ASTRON, Oude Hoogeveensedijk 4, 7991 PD Dwingeloo, Netherlands.
[7]Chalmers University of Technology, Onsala Space Observatory, S-439 92 Onsala, Sweden
[8]SRON Netherlands Institute for Space Research, PO Box 800, 9700 AV, Groningen, The Netherlands
[9]Centro de Astrobiologia, CSIC, Cra. de Ajalvir Km. 4, 28850 Torrejón de Ardoz, Madrid, Spain.
[10]Harvard-Smithsonian Center for Astrophysics, 60 Garden Street, Cambridge, MA 02138, USA
[11]Ghent University, Sint-Pietersnieuwstraat 25B - 9000 Ghent Belgium.
[12]KU Leuven, Institute of Astronomy, Celestijnenlaan 200d - box 2401, 3001 Leuven.
[13]TNO Optics, P.O. Box 155, 2600 AD Delft, The Netherlands.
[14]Stinger Ghaffarian Technologies, Inc., Greenbelt, MD,, USA.
[15] Steward Observatory, The University of Arizona, Tucson, AZ 85721, USA

2 OPTICAL DESIGN

2.1 Rationale

An IFU based design was preferred to a long-slit design for the MIRI Spectrometer for the following reasons.

Firstly, for point source observations, the need to centre the source in a narrow slit (via a peak-up procedure) is relaxed significantly, with the additional benefit that there is no loss of light at the slices ('slit losses' in a conventional long slit spectrometer). The MRS slice width is set to be less than or equal to the FWHM of the diffraction limited point spread function at the slicing mirror. An equivalent long-slit spectrometer would vignette the light outside this region, losing about 50% of the total.

Second, from a scientific perspective, the wavelength range covered by the MIRI spectrometer is sufficiently broad (a factor of nearly six) that different emission mechanisms may dominate in different regions of the spectrum. In cases where these mechanisms do not share a common centre (e.g., stellar output compared with infrared re-emission in a starburst galaxy), a simple slit spectrograph poses a dilemma in placing the "source" on the slit.

These considerations, combined with the wavelength coverage and resolving power requirements defined by the JWST mission science goals, and the mass, volume and electrical power limitations set by the JWST spacecraft environment, have resulted in a system with the characteristics summarised below and illustrated in block diagram form in Figure 1.

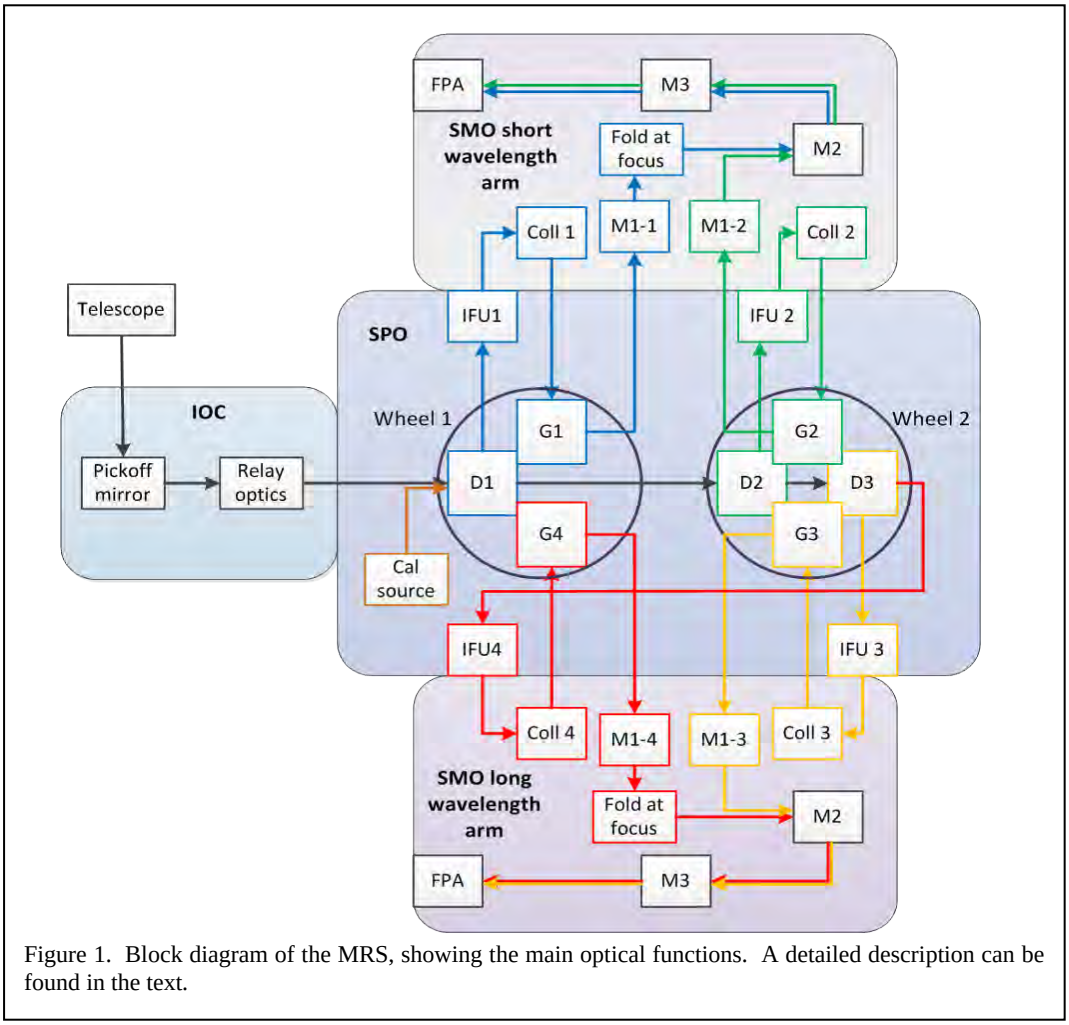

Figure 1. Block diagram of the MRS, showing the main optical functions. A detailed description can be found in the text.

As shown in the figure, the full 5 to 28.5 μm wavelength range is divided within the Spectrometer Pre-Optics (SPO) into four simultaneous spectral channels, each with its own IFU, and using a simple scheme of pass-band separation by dichroic filters whose design is described in Hawkins et al. (2007) and Wells et al. (2004). We denote the short and long wavelength limits of each channel as λ_{short} and λ_{long}. Each channel serves an optimised spectrometer.

This separation provides several benefits: it enables the use of diffraction gratings in first order, obviating the need for additional order separation filters; it also allows the IFU slice widths to be tailored to the wavelength scaled FWHM in each channel.

Electrical and thermal constraints limit the MRS to two 1024 x 1024 Si:As detectors (Ressler et al., 2014, hereafter Paper VIII), resulting in the spectrometer being split into two sets of optics, each with its own detector array, one for the two short-wave channels and one for the two long-wave channels. In each case, the spectra of two wavelength channels are imaged simultaneously onto the upper and lower halves of a detector array.

The product of spatial and spectral coverage that can be achieved in a single instantaneous exposure is ultimately set by the number of detector pixels. For the MRS, this results in a single exposure providing a spectral sub-band that covers only one third of each channel. Full wavelength coverage then requires three exposures, with a pair of mechanisms being used to select the gratings and dichroics in each case. We refer to the short and long wavelength limits of each sub-band as λ_{min} and λ_{max}.

This design choice allows the grating's performance to be optimised over a narrow wavelength range ($\lambda_{max}/\lambda_{min} \sim 1.2$). The gratings only have to work over 20% of the 1st order near the blaze wavelength and the dichroics do not have to be used near the cross over between reflection and transmission.

We will now step through the optical train as shown in Figure 1: the Input Optics and Calibration (IOC) modules pick off the MRS FOV from the JWST focal surface and pass it on to the SPO. The SPO spectrally splits the light into the 4 spectrometer channels and spatially reformats the rectangular fields of view into slits at the entrance of the Spectrometer Main Optics (SMO). The SMO comprises fixed optics that collimate the light for presentation to diffraction gratings mounted in the SPO and then re-images the dispersed spectra onto the two focal plane arrays. Key features of this optical system are described individually in the following subsections. The spectral and spatial coverage of the MRS is summarised in Table 1.

Table 1. Spatial and spectral parameters for the 4 MRS channels

Channel:			1	2	3	4
Slice width		arcsec	0.176	0.277	0.387	0.645
Number of slices		-	21	17	16	12
Slice width at detector for λ_{short}, λ_{long}		pixels	1.405, 1.791	1.452, 1.821	1.629, 2.043	2.253, 2.824
Pixel size along slice		arcsec/ pixel	0.196	0.196	0.245	0.273
λ/D at λ_{short}		arcsec	0.17	0.26	0.40	0.60
FOV: along slice × across slice		arcsec	3.70 x 3.70	4.51 x 4.71	6.13 x 6.19	7.74 x 7.74
Sub-band A	λ_{min}, λ_{max}	µm	4.87, 5.82	7.45, 8.90	11.47, 13.67	17.54, 21.10
	$R(\lambda_{min})$, $R(\lambda_{max})$	-	3320, 3710	2990, 3110	2530, 2880	1460, 1930
Sub-band B	λ_{min}, λ_{max}	µm	5.62, 6.73	8.61, 10.28	13.25, 15.80	20.44, 24.72
	$R(\lambda_{min})$, $R(\lambda_{max})$	-	3190, 3750	2750, 3170	1790, 2640	1680, 1770
Sub-band C	λ_{min}, λ_{max}	µm	6.49, 7.76	9.94, 11.87	15.30, 18.24	23.84, 28.82
	$R(\lambda_{min})$, $R(\lambda_{max})$	-	3100, 3610	2860, 3300	1980, 2790	1630, 1330

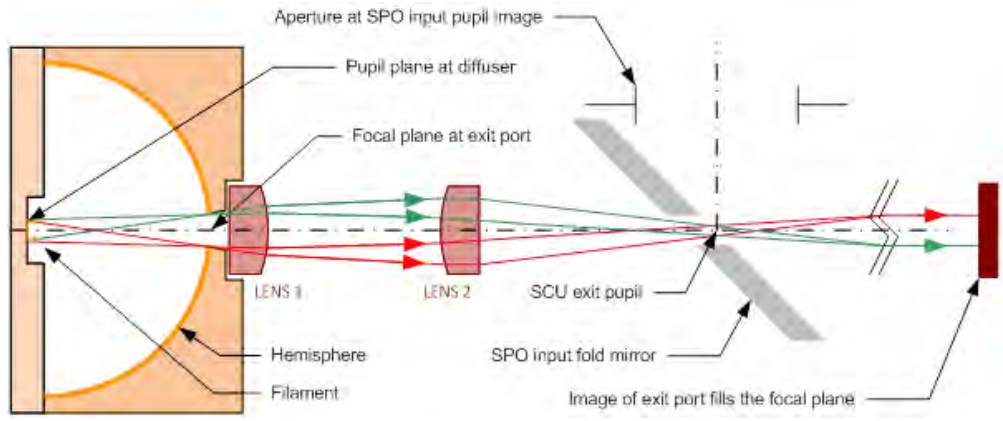

Figure 2. Optical Schematic (not to scale) of the Spectrometer Calibration Unit (SCU). Calibration light is injected via the obscuration at the centre of the JWST pupil where it is imaged at the input fold mirror of the Spectrometer Pre-Optics (SPO).

2.2 Telescope Focal Plane to Integral Field Units

The field of view of the MRS is adjacent to the MIRI imager field and picked off from the JWST focal surface using the MIRI Pickoff Mirror (POM) which is common to both. The sky and the JWST pupil are reimaged by the IOC so that there is a pupil image at the SPO input and a sky image further on. A cold stop that is 5% oversized with respect to the JWST pupil is placed at the SPO input pupil for straylight control.

The light is directed towards the first dichroic filter via a fold mirror placed 10 mm beyond the pupil. The focal plane is formed 535 mm beyond the pupil, providing the long path length and narrow beam waist needed between the pupil and the inputs of the four Integral Field Units (IFUs), for mounting a chain of dichroics to split the light between the MRS' four spectral channels.

A hole in the fold mirror, sized to be smaller than the footprint of the telescope central obscuration, acts as an aperture for the injection of light from the on-board Spectrometer Calibration Unit (SCU), shown in Figure 2.

The SCU provides spatially and spectrally uniform blackbody illumination for flux calibration and pixel flat fielding functions, using as its light source a tungsten filament heated to a temperature of ~ 1000 K by the application of an 8 milliAmp drive current. The filament is mounted inside a non-imaging flux concentrator that generates spatially uniform focal plane illumination at the exit port of a 25 mm diameter reflective hemisphere, (described in Glasse et al., 2006).

Two cadmium telluride lenses within the SCU then re-image the exit port onto the IFU input focal planes. The lenses provide a pupil image that coincides with the hole in the input fold mirror. This hole is positioned to lie within the footprint of the central obscuration of the JWST primary mirror and so has no impact on the science beam. In this way, the SCU can provide flood illumination of the full MRS field of view without any need for mechanisms or additional optical elements.

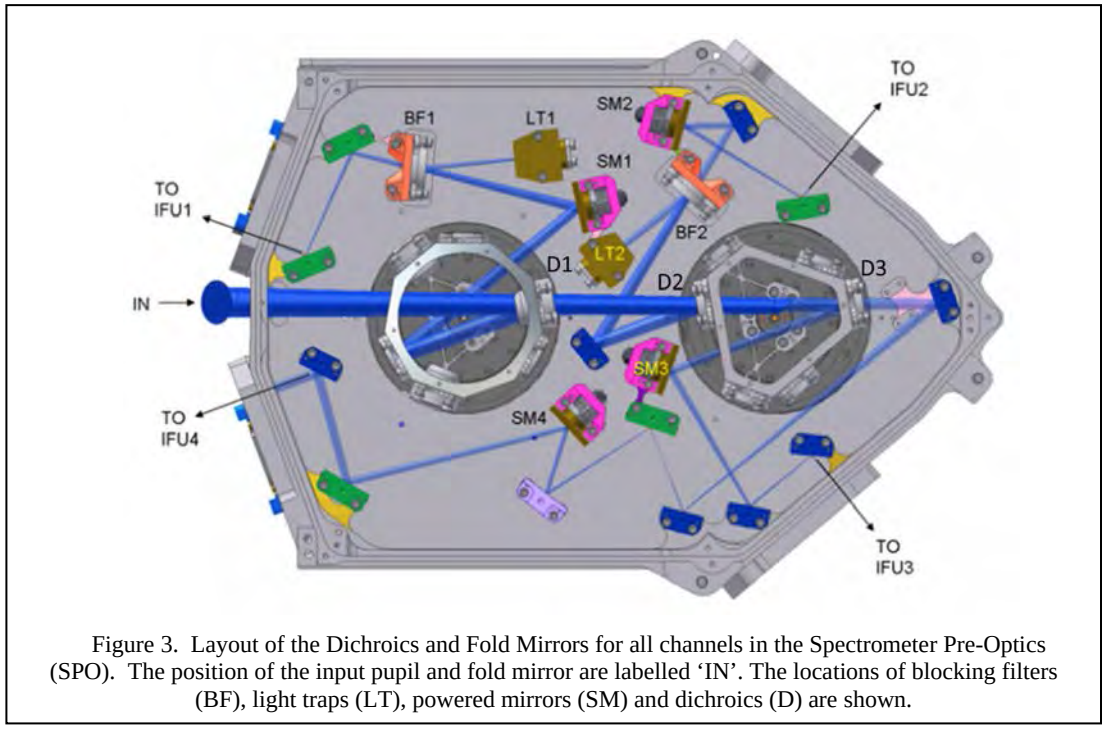

Figure 3. Layout of the Dichroics and Fold Mirrors for all channels in the Spectrometer Pre-Optics (SPO). The position of the input pupil and fold mirror are labelled 'IN'. The locations of blocking filters (BF), light traps (LT), powered mirrors (SM) and dichroics (D) are shown.

The overall layout of the dichroic assembly is shown in Figure 3, with the input fold mirror and SCU situated at the left-hand end (but not shown). The three dichroics needed to split the spectral band between the four spectrometer channels for one of the three sub-bands are indicated as D1, D2, and D3 in Figure 1 and Figure 3.

Taking Sub-band A as an example, the required reflective band for dichroic D1 is the wavelength range for Sub-band A in Channel 1, while its transmission band needs to extend from the short end of Sub-band A in Channel 2 to the long end of Sub-band A in Channel 4. The bands for which the mean reflectivity was above 0.95 and the mean transmission was above 0.74 are listed in Table 2 for all nine dichroics.

Table 2. Reflective and transmissive bands of MIRI dichroic beam-splitters.

Identification	Reflection Band (μm)	Transmission Band (μm)
Dichroic 1A	4.84 – 5.83	7.40 – 21.22
Dichroic 1B	5.59 – 6.73	8.55 – 24.73
Dichroic 1C	6.45 – 7.77	9.87 – 28.83
Dichroic 2A	7.40 – 8.91	11.39 – 21.22
Dichroic 2B	8.55 – 10.29	13.16 – 24.73
Dichroic 2C	9.87 – 11.88	15.20 – 28.83
Dichroic 3A	11.39 – 13.68	17.45 – 21.22
Dichroic 3B	13.16 – 15.80	20.34 – 24.73
Dichroic 3C	15.20 – 18.25	23.72 – 28.83

All of the gratings work in their first diffractive order so additional blocking is needed to reject second and higher orders. Because the dichroics work in series it is possible to use the combined blocking of dichroics 1 and 2 to remove the need for blocking filters in Channels 3 and 4. For Channels 1 and 2, dedicated blocking is provided by the fixed dichroics shown as BF1 and BF2 in Figure 3, with light traps LT1 and LT2 absorbing unwanted reflections.

The path length required to reach the input of Channel 4 is greater than the 535 mm discussed above, so the light transmitted by the final dichroic is re-imaged via an intermediate focal plane to the entrance of the Channel 4 IFU.

The 21 mm diameter dichroic filters are mounted on two wheels. First is the nine-sided wheel A containing the three Channel 1 dichroic filters and three flat mirrors to direct the light towards Channel 1. The second, six-sided wheel, contains the six dichroics needed to divert the light into Channels 2 and 3.

Each dichroic filter is mounted onto a diamond machined facet on the wheel that provides the required alignment accuracy and reduces the magnitude of any print-through of surface form errors from the wheel to the filter substrate. The filters are held in place with a spring loaded bezel with a clear aperture of 17 mm compared with the coated area of 17.4 mm. The bezel prevents light from reaching the uncoated area of the filter, which might result in un-filtered light entering the optical path. The blocking filters are mounted directly to the SPO chassis with a stand and bezel, similar to the mounting arrangement for the wheels.

The wheels also carry the corresponding diffraction gratings for each sub-band (three per channel), as discussed in Section 2.4. By arranging for the gratings to be mounted on the same wheels as their band-selecting dichroics, the number of moving mechanisms within the MRS is kept to two. However, before the light in the four channels reaches the gratings it is sliced and reformatted by the Integral Field Units and so we describe these next.

2.3 The Integral Field Units

The parameters pertaining to the spatial and spectral coverage and sampling of the spectrometer, which are largely determined by the design of the four IFUs, are given in Table 1. Spatially, the image is sampled in the dispersion direction by the IFU slicing mirrors and in the slice direction by the detector pixels. Spectrally, the width of the slices defines the spectrometer entrance slit and the width of the image (in pixels) of the slice at the

detector defines the width of the spectral sample. Inspection of Table 1 then shows that Channels 1 to 3 are all slightly undersampled spectrally, with slice widths less than 2 pixels at the detector.

The bandwidth of the spectral channels listed in Table 1 was chosen such that the ratio $\lambda_{long}/\lambda_{short}$ in all four channels was the same: $\lambda_{long}/\lambda_{short} = (28.3 / 5)^{1/4} = 1.54$. Each sub-band then has a width that is slightly larger than one third of its parent channel's band-width, where the excess provides sufficient overlap of adjacent spectra to allow their concatenation. In practice, the overlap is typically 10 to 15 % of the spectral range, depending on the specific sub-bands and position in the field of view.

For full Nyquist sampling of the telescope PSF the four IFU slice widths should ideally be matched to the half width at half maximum intensity of the PSF at the shortest wavelength in each channel. For the JWST telescope pupil this would equate to $a_{diff} = 0.088$ (λ_{short} / 5 μm) arcsec. However, the large increase in the beam size produced by diffraction at the IFU slicer mirror would necessitate large apertures for the spectrometer optics to avoid vignetting.

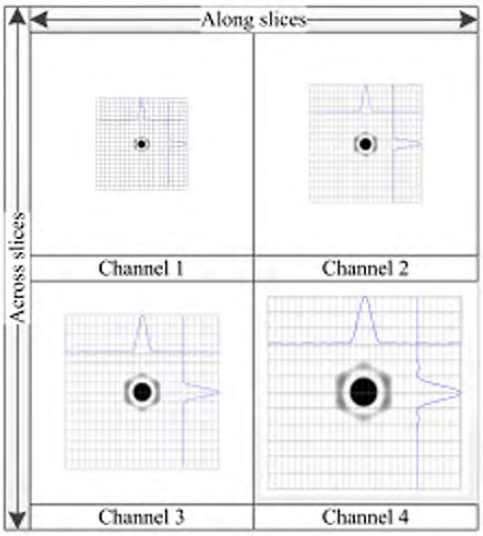

Figure 4. Nominal fields of view and sampling of the 4 IFUs. The JWST PSF at the shortest wavelength in each channel is overlaid by the sampling elements.

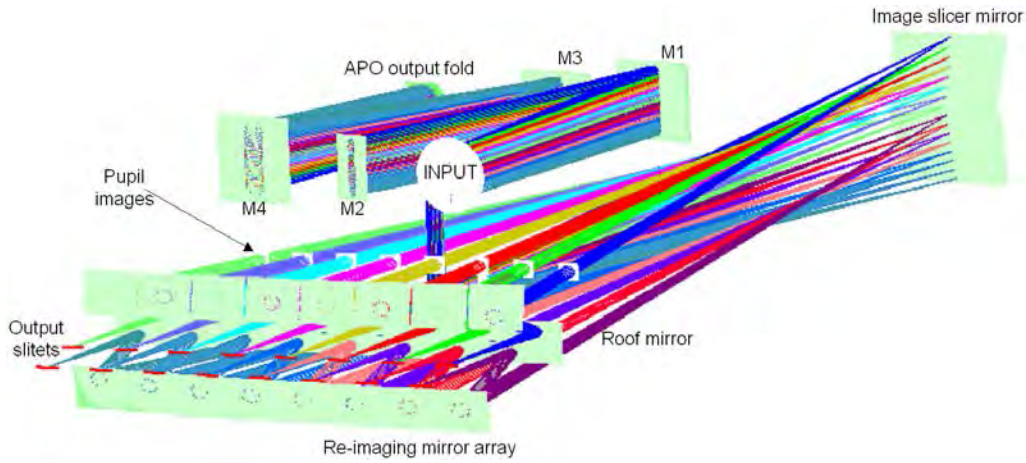

Figure 5. Three Dimensional View of the Channel 3 IFU. The slicer mirror is oriented with slice #1 at the top, nearest the APO and the corresponding slit #1 at the top right of the array of output slitlets.

To control the spectrometer's size, mass and optical aberrations, the starting point for determining the slice widths was to set them equal to 2 a_{diff}, with fully sampled PSFs to be achieved using 2 or more pointings of the telescope.

Optimum spatial sampling, which minimises the number of telescope pointings needed to fully sample all four channels simultaneously in the across-slice direction, then led us to adopt a set of slice widths that follow a scheme where the slices are factors of 1, 11/7, 11/5 and 11/3 wider than the narrowest 0.176 arcsec slice. These values allow full Nyquist sampling to be achieved using a single 'diagonal' offset whose magnitude in the across slice direction is equal to 11/2 times the width of the narrowest slice (0.97 arcseconds) and (N + ½) detector pixels in the along slice direction (where N is an integer).

The fields of view and PSFs (i.e., λ/D, which is roughly the FWHM of the PSF) at the shortest wavelengths for each channel are illustrated in Figure 4 where the size of the sampling elements listed in Table 1 are shown by the rectangular grid and the width of the PSF is plotted in cross-sections across and along the slices.

The optical path through the IFUs begins with the four toroidal mirrors, which comprise the anamorphic pre-optics (APO) module, as shown in Figure 5. The APO re-images an area of up to 8 by 8 arcseconds of the input focal plane (at the position of the white circle in Figure 5) onto the image slicer mirror, with anamorphic magnification. In the across slice (dispersion) direction one slice width is matched to the FWHM of the Airy pattern at the shortest operating wavelength for the IFU. In the along slice direction the magnification is chosen to provide the required plate scale at the detector. These two magnifications are not the same and so the APO exit pupil is elliptical, as illustrated in Figure 6, where the footprint of the JWST pupil is shown in blue.

The IFU design was developed from the IFU deployed in UIST, a 1-5 μm spectrometer for UKIRT (Ramsay-Howat 2006), and consists of an entrance pupil, an input fold mirror, an image slicer mirror, an exit pupil, two re-imaging mirror arrays, an output fold mirror and the exit slit mask. Each IFU takes the rectangular FOV

and transforms it into a pattern of slitlets (shown in red in Figure 5) at the entrance aperture for its corresponding grating spectrometer.

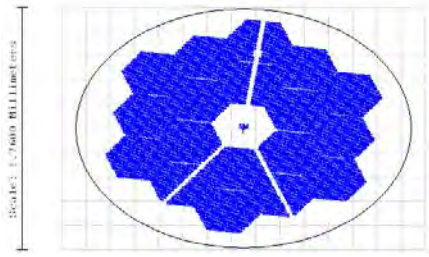

Figure 6. Rotated and anamorphically magnified pupil image at the entrance to the IFU, plotted on a square grid.

The slicing mirror comprises a number of spherical optical surfaces, diamond turned onto a common substrate. Figure 7 is a photograph of the image slicer mirror for Channel 1, which has 21 slicer mirrors arranged about the centre of the component with 11 slices on one side and 10 on the other. Each mirror is offset to direct its output beam towards the corresponding re-imaging mirror. The design for channels 2 to 4 is similar but with correspondingly fewer larger slices as the wavelength increases, as listed in Table 1. The mirrors are arranged in a staircase-like manner to aid manufacturing.

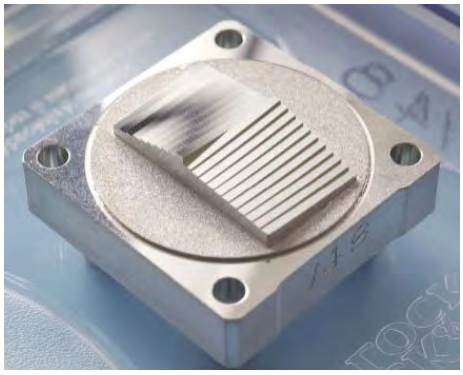

Figure 7. Photograph of the Channel 1 Image Slicer Mirror (Courtesy of Cranfield University).

Each of the slices re-images the IFU entrance pupil at a scale of ≈1:1 and because the centres of curvature of the mirrors are offset laterally with respect to each other, the pupils that the slices produce are separated, as can be seen in Figure 5.

The slicing mirrors truncate the anamorphically magnified image of the sky along the dispersion direction, as shown in Figure 8 (a) to (c). This truncation results in the pupil image being diffraction broadened in the dispersion direction as shown in Figure 8 (d). To reduce vignetting, the baffle at this pupil image and subsequent optical components (including the diffraction gratings) are oversized. This is illustrated in Figure 8(d) where the geometric footprint for 3 field positions are overlaid along a slice to appear as the blurred green patch in the image. The notional, geometric pupil is shown in red and the oversized mask aperture is shown as a green rectangle.

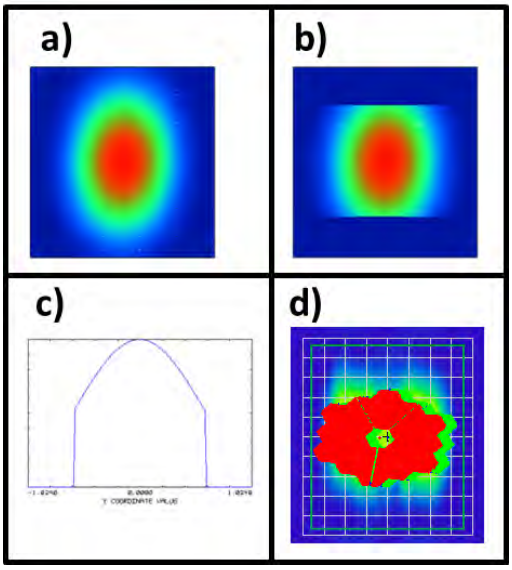

Figure 8. (a) and (b), Input and truncated images on the imager slicer mirror. (c), Cross-section through the peak of the truncated image. (d), Diffraction broadened pupil images (see text for details).

The re-imaging mirror array in Figure 5 forms images of the slicing mirrors as input slits of the spectrometer and also image the pupils at infinity, making the output telecentric. Finally, a roof mirror redirects light from the re-imaging mirrors so that the output consists of the two lines of staggered slit-lets seen in Figure 5.

A slotted mask at the position of the IFU output slits defines the field of view along the individual slices, while in the spectral direction the slots are oversized to ensure they do not vignette the image, but still act as a baffle to reduce scattered light between the slices.

The number of detector columns covered by the four IFUs are approximately 476, 464, 485, 434 for channels 1 to 4 respectively. The size of the gap between individual slits for channel 1 is set to be approximately equal to the diameter of the first dark diffraction ring in the telescope PSF, (about 4 pixels). For channels 2 – 4 the size of the gap is slightly greater than the diameter of the first dark ring.

2.4 The Spectrometer Main Optics (SMO)

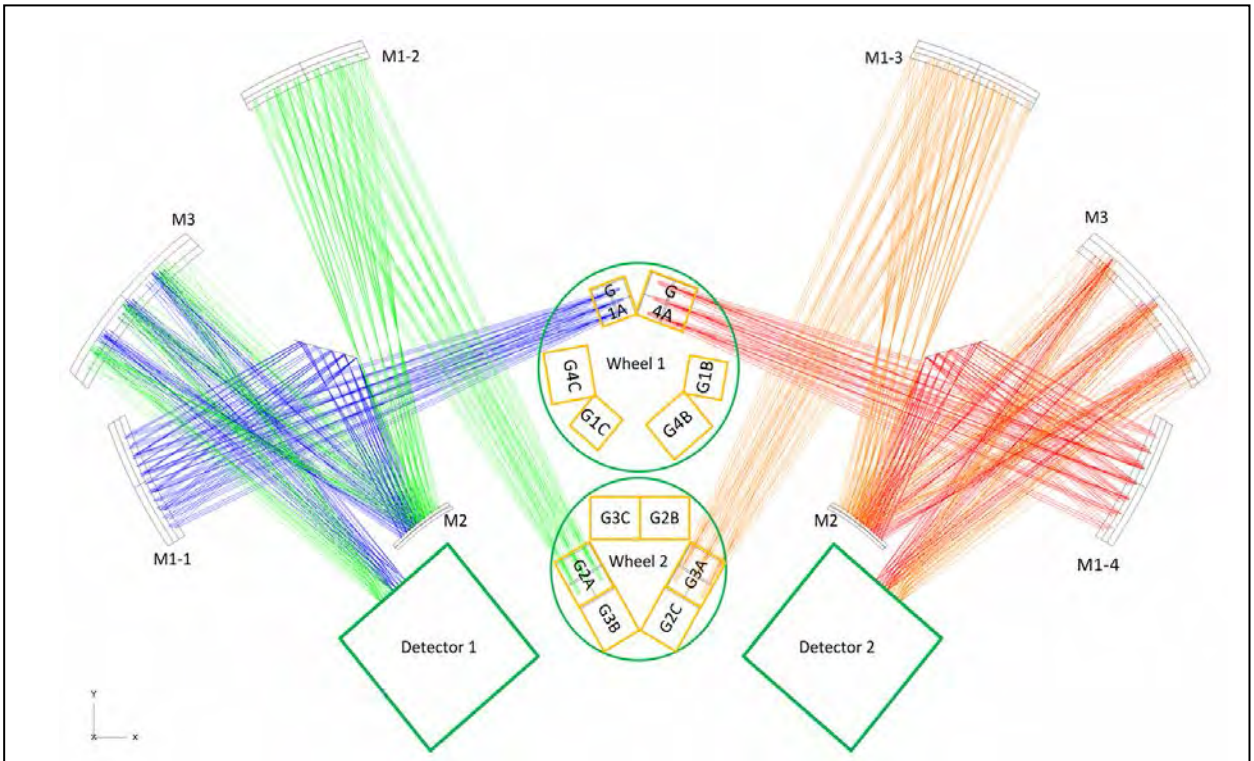

Figure 9. SMO cross-section of the camera symmetry plane in the spatial direction. Light arrives at the gratings (G1A, G2A, G3A, G4A) from the IFU output collimating mirror.

The SMO (whose layout is shown in Figure 9), comprises four grating spectrometers in two arms. Each spectrometer performs three functions – collimation of the telecentric output beams of one of the four IFUs, dispersion of the collimated beam and imaging of the resulting spectrum on to one half of one of the MRS' two focal plane arrays. One of the two spectrometer arms includes the two short wavelength channels (1 and 2), and the other the long wavelength channels (3 and 4). We will now step through the optical path for a single channel from the IFU to the detector.

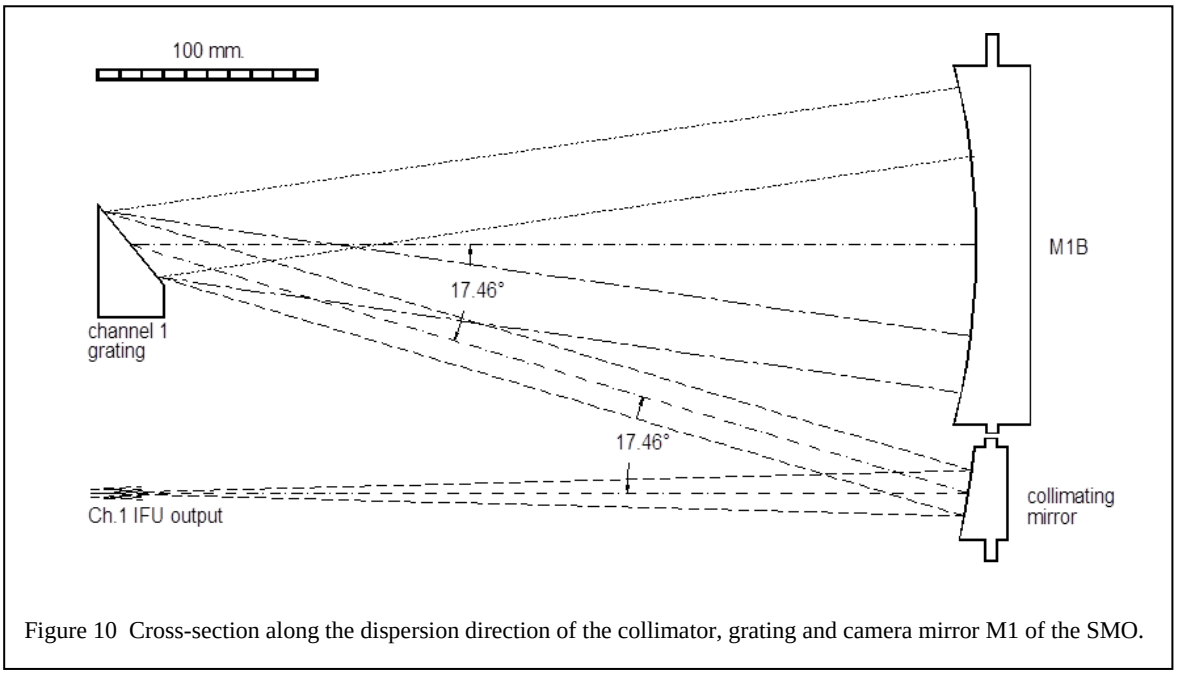

Figure 10 Cross-section along the dispersion direction of the collimator, grating and camera mirror M1 of the SMO.

The IFU output beam for each channel is collimated and its light directed towards the corresponding diffraction gratings as shown in Figure 10.

Figure 9 then shows the optical paths from the gratings to the detectors. The channels have separate, but identical, M1 camera mirrors that provide an intermediate image of the spectra. The spectra for channels 1 and 2 and channels 3 and 4 are combined into

a single image at this intermediate focus by reflecting the channel 1 and channel 4 spectra towards M2. The combined pairs of channels are then imaged side by side on to the detectors by the M2 and M3 mirrors in each arm of the SMO.

Figure 11. Grating Wheel Assembly (Wheel 1).

The gratings for the A, B and C sub-bands are mounted on the wheels that also carry the dichroics on a lower level. The wheels are located in the SPO and are rotated together by a single mechanism to give the correct combination of dichroics and gratings across all channels for each exposure.

Table 3. MRS grating dimensions; groove length (Len), ruled width (Wid.), angle of incidence (Inc.) and angle of diffraction (Diff.).

Ch.	Band	Grating Constant [mm^{-1}]	Len. [mm]	Wid. [mm]	Inc. [deg]	Diff. [deg]
1	A	266.67	28	44	55.46	29.2
	B	230.77				
	C	200.00				
2	A	171.43	30	63	54.46	28.5
	B	148.45				
	C	128.57				
3	A	12.06	30	63	54.46	28.5
	B	96.97				
	C	83.96				
4	A	71.43	34	64	53.46	27.2
	B	61.28				
	C	52.55				

The mirror substrates are all light-weighted aluminium with diamond turned optical surfaces that are gold coated for maximum reflectivity at the MIRI operating wavelengths. They are mounted through holes in the housing walls using strain relieving lugs under light tight covers to prevent any high temperature radiation from the instrument enclosure (at ~40 K) reaching the detectors.

The gratings are master rulings on aluminium substrates and are gold coated. They are mounted on to grating wheel assemblies as shown in Figure 11.

Table 3 lists the design parameters of the gratings. The ruling frequencies are chosen to be easy for manufacture by direct ruling, by using fractions of 3600 to give a minimum (< 1 %) degradation in performance. All gratings operate in their first order. The angular values quoted in Table 3 are calculated for the (virtual) nominal input beam, originating from the centre of the IFU output area.

2.5 Stray Light Control

The SPO is designed to be a well baffled optical system, with aperture masks in five locations. To intercept stray light, a cold stop at a pupil in the SPO constrains the entrance pupil to the MRS. The MRS also has a number of features to control stray light: 1.) stops at each pupil and sky image in the optical train; 2.) light traps where significant stray light occurs (0^{th} order from the gratings); 3.) labyrinths at the edge of apertures between modules and tight control of all external apertures, e.g. electrical feed throughs; 4.) black coating of all surfaces not in the main optical path; and 5.) avoidance of surfaces at grazing incidence near the main optical path. In addition, for each IFU each slice there are output pupil and slit masks.

All the diamond turned aluminium mirrors in MIRI were specified to have a surface roughness of <10nm RMS. This results in a total integrated scatter per surface of <0.06%; non-sequential optical modelling indicated that this level of scatter should not significantly degrade the PSF of either the MIRIM or MRS. Measurements of images in the MIRIM show this to be the case. For the MRS there is some scattered light (Paper VI) caused by the SMO optics; it has been modelled sufficiently accurately to allow removing its signal during data reduction. All mirrors have an overcoated gold surface

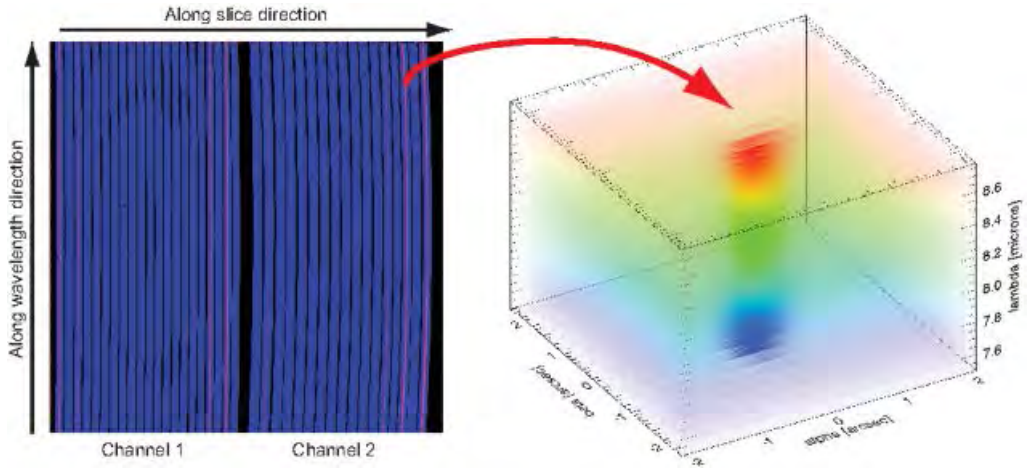

Figure 12. Illustration of the reconstruction process: The detector image for two channels is reconstructed into a 3D cube with two spatial dimensions (α along the slice and β across the slice) and one spectral dimension (λ).

with reflectivity >98.5% in the MIRI wavelength range.

Straylight analysis shows that the extensive baffling combined with the low scattering optical surfaces and blackened structure reduce unwanted light (cross talk between channels, degraded PSF and out of beam light at the output image) to levels that are estimated to be less than 0.1 % of the thermal background radiation included in the science beam.

3 MEASURED PERFORMANCE

3.1 The Spectral Image

Due to the nature of an IFU spectrograph with its slicing and dispersing optics, the resulting detector images are not straightforward to analyze: Spatial, spectral, and with it photometric information, are spread over the entire detector array. Further, the gratings are used in an optically fast, non-Littrow configuration. The resulting anamorphic magnification varies from the short to long wavelength limit for each sub-band, making optical distortion significant and complex, with the dispersed slices forming curved images on the detector as shown in Figure 12.

The slicing optics add another component of distortion that varies the plate scale in the along-slice direction for each slice individually. This leads to a very complicated variation of the spatial plate scales and finally to a dependency of the spatial and spectral axes on each other and on the location on the detector array.

To enable scientific studies based on MRS data, the flux measured in each detector pixel needs to be associated with a wavelength and location on the sky. Since the IFU provides two spatial dimensions, each detector pixel corresponds to a three-dimensional cube with two spatial and one spectral dimension. Due to the optical distortion, the edges of these cubes are neither orthogonal nor constant in length. Consequently, we have developed a process (called image or cube reconstruction), which allows a transformation of the detector pixels into an orthogonal cube.

Cube reconstruction requires a thorough understanding of the optical distortion. It is not possible to just characterize the curved images of the dispersed slices (as shown in the left plot of Figure 12), by approximating the curvature with polynomial functions. Due to the distortion caused by the slicing optics, the spatial plate scale varies within a slice non-uniformly. The characterization of the plate scale and the association of each detector pixel with its projected location in the sky at any given wavelength is a task for the astrometric and wavelength calibration, described in the next sections. Once the sky-coordinates and wavelength are known for each detector pixel, the cube can be reconstructed as discussed by Glauser et. al. (2010).

3.2 Astrometric Calibration

To describe the optical distortion on the image plane of the detectors we began from the optical model, using ray-tracing techniques to project each detector pixel through the slicing optics backwards onto the sky. When the as-built geometry was taken into account, we achieved a high spatial accuracy, as demonstrated for the MIRI Verification Model (Glauser, et al., 2010). To verify this approach, a dedicated astrometric calibration campaign was conducted during the instrument test campaign of the MIRI Flight Model.

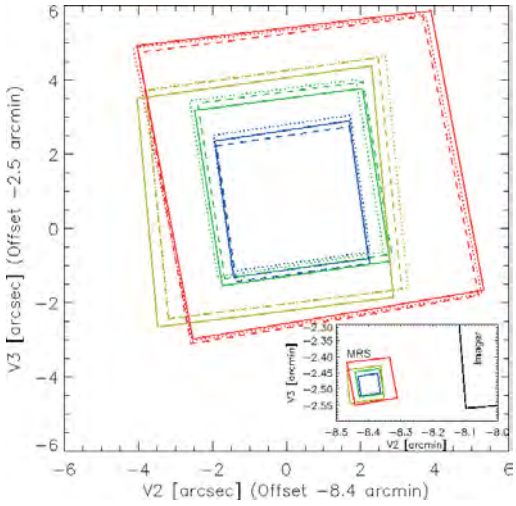

Figure 13. Transformed MRS fields in the JWST coordinate frame (V2, V3). The field borders are drawn as solid lines (Sub-band A), dashes (Sub-band B) and dots (Sub-band C) for channel 1 (blue), 2 (green), 3 (yellow) and 4 (red). The inset shows the position of the MRS FoV relative to the imager field.

As outlined in Glauser et al. (2010), the intra-slice spatial distortion can be approximated with a 2nd order polynomial to accuracies of a few milli-arcseconds - much better than required for the astrometric accuracy given the minimum plate scale of 0.196 arcseconds in the along-slice direction for channel 1. We conducted the astrometric calibration by placing a broad-band point source at three field positions for each slice and each channel and recording the dispersed signature on the detector. The central pixel of the spatial profile was determined and correlated with the known position of the point source (our reference on the sky). With this method we were able to determine the spatial plate scale at any location on the detector. Due to limitations of the test setup, i.e., strong field distortion of the steerable point-source, the achievable relative astrometric accuracy was very limited. However, within an estimated upper limit of ~0.5 pixels (0.098 arcsecond for channels 1 and 2, 0.123 arcsecond for channel 3, and 0.137 arcsecond for channel 4), the approach of using the optical model for the reconstruction was validated.

A further result from this calibration campaign was the measurement of the FOV for each sub-band. Figure 13 shows the MRS FOV in the JWST coordinate frame and its position relative to the imager field. The FOV common to all MRS channels is 3.64 arcsec in the along-slice (α) and 3.44 arcsec in the across-slice direction (β).

3.3 Wavelength Calibration

To determine the absolute wavelength of the MRS channels we conducted a series of calibration measurements during the instrument test campaign. Fabry-Pérot etalon filters were used to create a dense pattern of unresolved spectral lines on the detector. Many tens of lines were typically visible at a signal to noise ratio of more than 50 in a single sub-band exposure. To provide a reference wavelength to distinguish between adjacent etalon lines, the telescope simulator used in the test was also equipped with a pair of 'edge' filters, one of which cut-on at around λ = 6.6 μm (in Sub-band 1C) and the other which cut off at λ = 21.5 μm (in Sub-band 4B).

The absolute wavelengths of the etalon lines and edge filters had previously been measured at ambient and 77 K temperatures using a laboratory standard Fourier Transform spectrometer with a spectral resolving power of R = 100,000. The extrapolation of the wavelength

scale to the 34 K operating temperature for the test campaign was based on published measurements (Browder and Ballard, 1969, Browder and Ballard, 1972 and Smith and White, 1975). This extrapolation resulted in a typical wavelength correction of less than 1 % of the width of the MRS spectral resolution element.

The wavelength calibration process then involved the assignment of an absolute wavelength to an etalon line by fitting the calibrated spectra of the edge filters to their MRS measured spectra in Sub-band 1C and 4B. The known separation of the etalon lines was used to extend the wavelength scale across the full spectral image. To extend the scale to other Sub-bands, pairs of measured etalon spectra were co-added and the position of unique identifying features due to spectral beating between the two patterns was used. A set (2 per sub-band) of second order polynomial fits to the positions of the etalon lines was used to generate a wavelength value for the corners of all illuminated pixels.

The wavelength calibration derived in this way was encoded for use in the MRS calibration pipeline by forming six images (one for each MRS detector and all three grating wheel settings) where the image signal values were set equal to the wavelengths at the corner of each detector pixel. We note that as a result, these wavelength reference images have one more row and column than the detector images.

The relative accuracy of this wavelength scale (within and between sub-bands) is estimated to be better than 0.02 spectral resolution elements which, for example, corresponds to 0.03 nm at λ = 5 μm. The absolute accuracy of the wavelength scale is estimated to be comparable to this figure but this will need to be confirmed during on-orbit commissioning using spectral standards.

The wavelength calibrated etalon spectra were also used to measure the spectral resolving power of the MRS. The results are shown in Figure 14, where the sub-band averaged values are shown in red and the spread of values seen across the field of view is indicated by the black band.

We note that Figure 14 does not take account of the intrinsic spectral width of the etalon features, which was determined using the R = 100,000 calibrated spectra, described above. Initial efforts to deconvolve the intrinsic line profiles from the MRS measured spectra suggest that the resolving powers quoted in Figure 14 may be underestimated by around 10 %. We have therefore used the band averaged measurements scaled by a factor 1.1 to generate the summary values quoted in Table 1.

3.4 Spatial Sampling

As outlined in Section 2, the PSF of the MRS is under-sampled by design, with full sampling in both spatial and spectral dimensions requiring that the object be observed in at least two dither positions that include an offset in the across-slice direction of 11/2 times the channel 1 slice width (which corresponds to 7/2 slices in channel 2, 5/2 slices in channel 3, and 3/2 slices in channel 4). Due to the curved shape of the distorted spectrum on the detector and the variable plate scale along the individual slices, the exact dither offset in the along-slice direction is less well determined (but also less critical). An intrinsic dither is provided with respect to

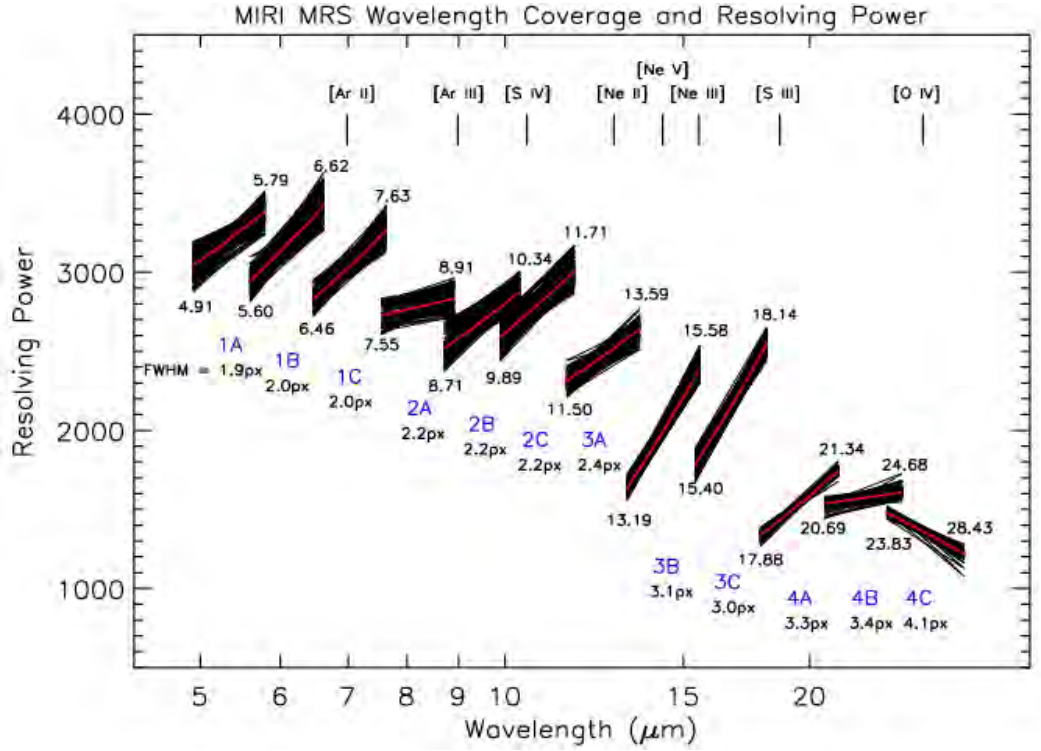

Figure 14. The spectral resolving power of the MRS. The black regions represent variations in the resolving power across the FOV for each sub-band, and the red lines are spatially averaged values. The wavelength ranges of each sub-band are indicated, as well as some scientifically important spectral lines. The mean width (FWHM) of the spectral resolution element in pixels is also provided for each sub-band.

the detector pixels due to the curvature of the dispersion profile. Figure 15 shows the nominal MRS dither pattern to be used in a single observation to sample point sources fully, as derived during test campaigns, and as proposed for in-flight operations.

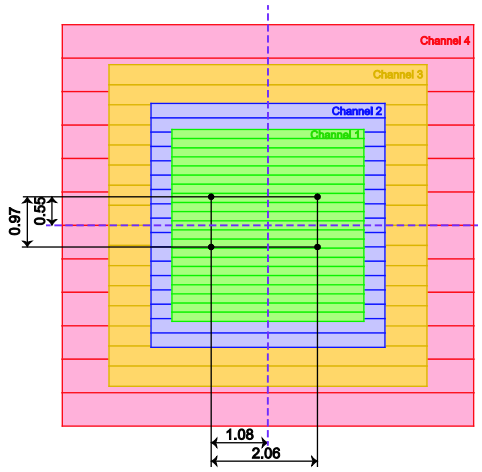

Figure 15. Coordinates in arcsec of the four nominal dither positions relative to the centre of the MRS field (dashed axes).

To achieve a fully sampled PSF, these dithered observations must be combined. We anticipate that this could most readily be achieved using the reconstructed cubes. To avoid loss of spatial resolving power caused by any shift- and co-adding algorithm due to the re-binning of the data (for example, Fruchter & Hook, 2002), we minimize the necessary re-binning steps by incorporating dither offsets parallel to the slice into the reconstruction algorithm itself. This has the advantage that only one re-binning step is required from detector data to reconstructed cubes, while dither offsets in the across slice direction can be corrected and combined afterwards using an interlacing method. Note that this is work in progress and we expect some more advanced techniques (such as drizzling, Fruchter & Hook, 2002) to be incorporated into the data reduction pipeline before launch.

3.5 PSF and Optical Quality

We attempted to measure the MRS PSF during flight model testing at RAL using the MIRI Telescope Simulator (MTS), described in Wright et al, (2014, Paper II). However, optical aberrations and vignetting in the MTS led to the expected point source being elongated and extended at short wavelengths, such that it did not provide a sufficiently point-like image. Even at longer wavelengths, where aberrations became less dominant as diffraction started to dominate, the measured PSF was broader than nominal due to vignetting in the telescope simulator.

We therefore repeated the PSF measurement on the flight model during the first cryo-vacuum test campaign at NASA-Goddard (CV1RR), where a compact and well defined point source was available. Deep exposures at 17 different locations in the MRS field were combined and reconstructed to form the PSF image for Channel 1A, shown in Figure 16. For these data, the spectral coverage was limited to a narrow (0.125 μm wide) wavelength range around 5.6 μm.

A comparison with the model PSF (pure diffraction limited Fourier-transformed JWST pupil) shows a very good match across the slices. In the along-slice direction, a broadening of approx. 50% is observed. Currently, possible causes considered for the broadening include scattering in the detector substrate (the detector halo effect, which is also observed in the imager and is discussed in Rieke et al., (2014, Paper VII) or a side-effect of the straylight discussed in Section 3.9. In the case of the halo effect, the larger degree of broadening seen in the MRS may be due to the larger spatial sample per pixel. More detailed modelling is required to confirm the root cause.

3.6 Spectral Fringing

Spectral fringes are a common characteristic of infrared spectrometers. They originate from interference at plane-parallel surfaces in the light path of the instrument. These surfaces act as Fabry-Pérot etalons, each of which can absorb light from the source signal with a unique fringe pattern. In the infrared wavelength range, surfaces separated by a fraction of a mm up to a few cm may form very efficient etalons. The most obvious source of fringes in the MRS is the detector itself with a physical thickness of 500 μm (Paper VII). Similar fringes have also been observed in spectra measured with the MIRI Verification Model during testing and with the Spitzer-IRS instrument, which employs comparable (though smaller) Si:As BIB detectors, Lahuis & Boogert (2003).

For the initial analysis we follow the formalism as defined in Kester et al., (2003); Lahuis & Boogert, (2003). The sine approximation, $I_t = A_f \cos(2\pi\omega D) + B_f \sin(2\pi\omega D)$, is used with ω being the wavenumber and D the optical thickness of the instrument component. Of primary interest to help in the identification and first characterization of the fringes is the optical thickness D. In the MRS test data three distinct fringe components are seen, with key parameters listed in Table 4.

Table 4. Observed fringe components with basic parameters and identification. The dichroic is modelled as Chemical Vapour Deposited CdTe.

#	Optical thickness [cm]	$\delta\omega$ [cm^{-1}]	Fringe origin	Peak to peak amplitude [%]
1	0.35 ± 0.02	2.8 (±0.2)	Detector substrate	d 40
2	2.7 ± 0.2	0.37 (±0.03)	Dichroic	d 10
3	0.01 to 0.1	10 to 100	Fringe Beating	d 10

Of the three fringe components two are directly matched to optical components in the instrument. The main fringe component (#1 in Table 4) has a derived optical thickness of approximately 3.5 mm for all sub-bands. This corresponds to the optical thickness of the detector substrate which has d ~ 500 μm and n ~ 3.42, giving D ~ 0.34 cm. Figure 17 gives an illustration of this fringe pattern, showing the main detector and dichroic fringes in more detail for Channel 4.

The optical thickness derived for the second, high frequency, component (D ~ 2.7 cm) is matched to that of the CdTe Dichroic filters (Section 2.2). For the third set of low frequency, components (D = 0.01 to 0.1 cm) no unique surfaces in the instrument are identified, instead these are likely to originate from beating between primary fringe components. The fringe variations come from the layered structure of the detector substrate and optical thickness differences between individual dichroic filters.

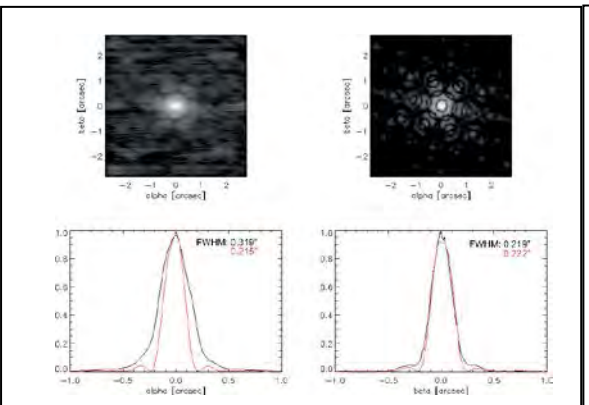

Figure 16. Measured PSF at 5.6 μm (top left) compared with the FFT of the JWST pupil (top right) and normalized peak profiles of the measured (black) and modelled (red) for the along-slice (bottom left) and across-slice direction (bottom right).

Figure 18 shows the peak normalized fringes over the entire wavelength range of the MRS. The two curves in Figure 18 show predictions for the expected fringe amplitudes based on representative anti-reflection (AR) coating profiles as applied to the MIRI flight detectors. The solid curve assumes a pure two-sided etalon while the dashed-dotted curve simulates a back-illuminated surface with a fully reflective front surface and photon absorption in the active layer (adopted from Woods et al., 2011). Though not a perfect match, this approximate detector model does reproduce the general trend and magnitude of the fringes.

Fringe removal will be achieved using the techniques developed for and applied to ISO and Spitzer data (see Lahuis & van Dishoeck, 2000; Kester et al., 2003; Lahuis & Boogert, 2003). This involves dividing the observed spectra by a fringe flat-field followed by the removal of fringe residuals using the sine fitting method. This approach has proven to be reliable and robust for most spectra and the experience with ISO and Spitzer has shown that it allows the removal of fringe residuals down to the noise level. The main limitations with this technique are the definition of the spectral continuum in the presence of spectral features and isolating the fringe spectrum from broad molecular (vibration-)rotation bands (e.g. C2H2, HCN, CO2 and H2O).

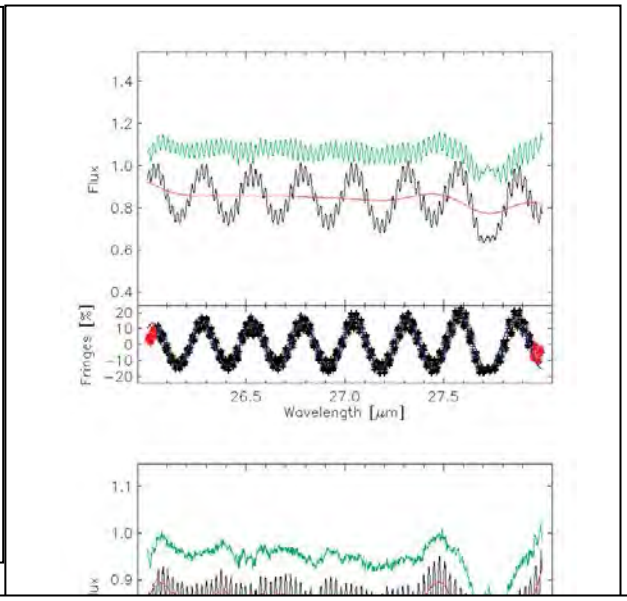

For the MIRI IFU other effects play a role and may limit the fringe removal for (near) point source measurements. The two major effects are; i) the

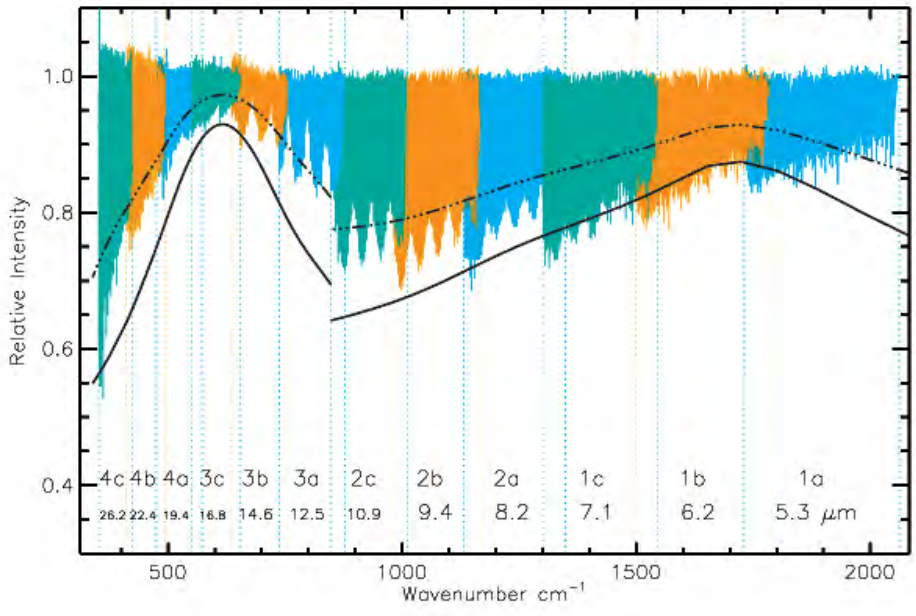

Figure 18. The combined fringes for each channel and sub-band. The data for each neighbouring band are plotted in a different colour for clarity. The main and high frequency fringe components are not resolved on this scale. In Channels 2 and 3 an example of a low frequency beating fringe can clearly be seen. Note: the spectrum is normalized to the peaks of the main fringe amplitude. See text for a description of the solid and dashed-dotted lines.

illumination (and its effective angle) on the detector depends on the source morphology (position and extent) and ii) the wavelength depends on the spatial location of the point source in the IFU field. This results in i) changes in the effective optical thickness from source to source and ii) a wavelength shift with spatial offset. Both modify the detailed fringe pattern for individual cases. Figure 19 illustrates this with point source measurements from the CV1RR test campaign and using extended source blackbody spectra from flight model testing at RAL. Small sub-pixel pointing offsets are seen to have a discernable impact on the fringe pattern.

For MIRI an alternative model-based approach is under study which uses the observed source morphology to define the fringe spectrum. This method will be applicable to both the MRS and the LRS, and will complement the traditional fringe removal techniques. This requires both a well-defined and well-calibrated fringe model (an ongoing MIRI team activity) and a flexible and iterative reduction pipeline (in development at STScI based on input from the MIRI team).

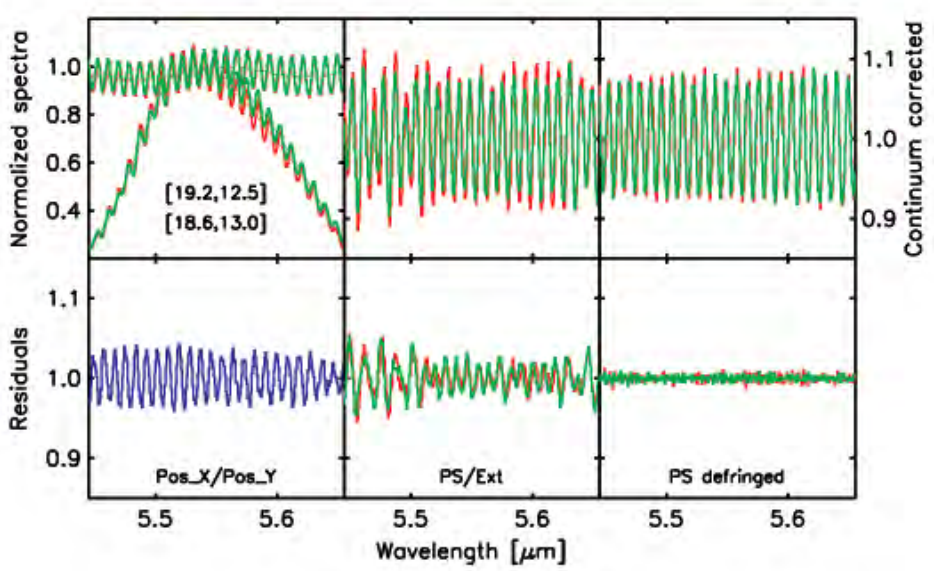

Figure 19. Illustration of the fringe source dependence for point and extended blackbody source spectra at two positions (red and green spectra) as printed in the top-left panel. Top from left to right; peak normalized point and extended spectra; normalized point source spectra; normalized extended blackbody spectra. Bottom from left to right; both point source spectra divided; point source spectra divided by extended source spectra (akin to direct flat-field correction); both normalized point source spectra de-fringed using a sine fitting technique.

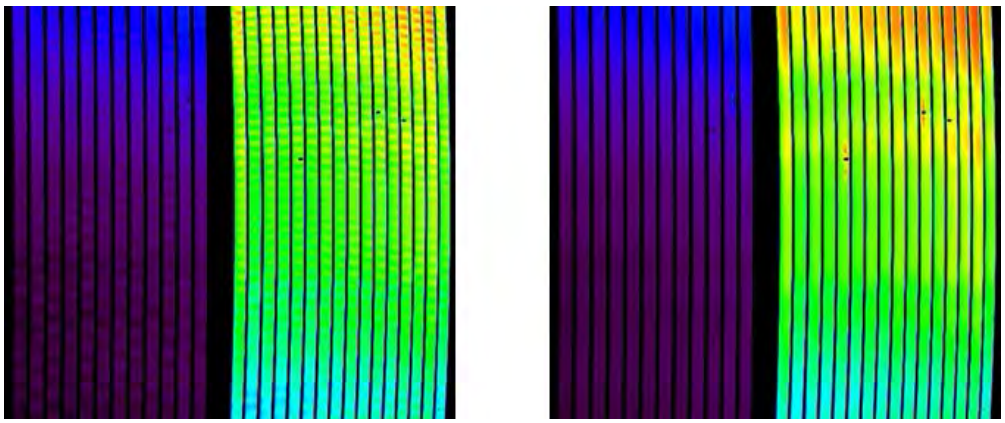

Figure 20. A sample of MRS data showing the effects of the fringes (left panel) and after the fringe correction (right).

These effects can be mitigated by traditional fringe removal techniques using optimized and iterative reduction algorithms (e.g. by modifying, shifting and stretching the reference fringe spectrum before applying it). This has been used in individual ISO and Spitzer cases and the MIRI team will work on developing optimized methods for the MRS.

3.7 Pixel flat field

We determined the pixel-to-pixel variation of the response for both short and long wavelength detectors, using measurements taken during testing at RAL. The illumination was provided by an external, extended source in the MTS. A number of exposures measured

over the period of the whole test run and covering the full MRS wavelength range were included in this calculation.

We first de-fringed the data using the prescription described in Section 3.6, with the results shown in Figure 20. We then calculated the mean value of each pixel, $f_{ave}(i,j)$, by averaging over 5 x 5 pixel boxes centered on pixel (i,j) and accounting for pixels close to the edges of the slices or near bad pixel clusters. The original data was then divided by these averaged values to create a map of the normalized pixel gain. We checked the distribution of the pixel-to-pixel variation for each exposure of all the available data for both detectors and all the sub-bands and found that the distribution is Gaussian with a full-width-half-maximum of ~2 % (Figure 21). The variation between different datasets has a standard deviation of d 0.2% for 16 different observations. The pixel-to-pixel variation does not appear to be wavelength dependent as both short and long wavelength detectors show the same overall flatness. This uniformity suggests that the correction of pixel response variations on orbit can be achieved using infrequent calibration measurements (no more than weekly, if the instrument is undisturbed).

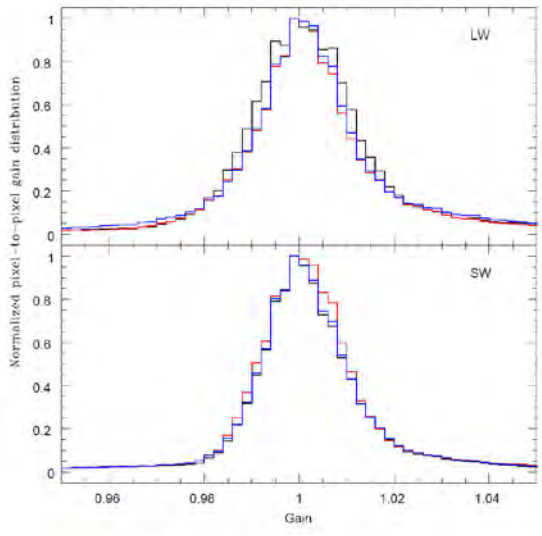

Figure 21. Normalized pixel-to-pixel gain distributions derived from 3 observations for SW and LW detectors (black, red and blue). The FWHMs are 1.91 % and 1.99 % for the SW and LW channels, respectively.

3.8 Spectrophotometric Performance

A spectrophotometric calibration for the MRS was derived during testing at RAL. This was done by configuring the MTS to provide extended illumination of the MIRI entrance pupil with the spectral energy distribution of a blackbody of 400, 600 and 800 Kelvin. For each MTS blackbody configuration, MRS spectra were obtained in all 12 spectral bands, together with background measurements using the blank position in the MTS filter wheel.

The data were processed using the standard DHAS tool (Paper II), which converts the raw readouts of the integration ramps to slopes in physical units (V/sec). The DHAS miri_cube module, which performs the reconstruction technique described in Section 3.1, was then used to construct spectral cubes from the slope images, re-gridding the focal plane array pixel signals onto an equidistant spectral cube The spectral cubes of the background measurements (MTS filter blank position) were subtracted from the flood illumination measurements to correct for the test facility background.

The absolute responsivity of the MRS is expressed in terms of the quantity referred to as the Photon Conversion Efficiency (PCE), which is equal to the number of electrons detected by the focal plane array for each photon incident at MIRI's entrance focal plane.

The spectral cubes produced with the DHAS miri_cube routine have a fully calibrated WCS with the plate scale and wavelength coverage of every cube pixel. When combined with an estimate for the absolute flux delivered to the entrance focal plane by the MTS (Paper II), this allows us to calculate the photon conversion efficiency in every pixel of the spectral cube for all MRS spectral bands. Table 5 lists the mean PCE for all MRS bands. We estimate the fractional error to be 20 % in these figures, due to systematic effects, primarily in estimating the absolute flux from the MTS.

Table 5. Mean photon conversion efficiency for all MIRI MRS bands. The PCE was averaged over all reconstructed spectral cube sample elements and all wavelengths.

Mean PCE [electron / photon]		Band		
		A	B	C
Channel	1	0.117	0.117	0.138
	2	0.114	0.130	0.134
	3	0.115	0.108	0.114
	4	0.028	0.020	0.011

One obvious feature of Table 5 is the sharp drop in PCE from Channel 3 to Channel 4. This is roughly a factor of 2.5 lower than was expected from sub-system measurements of the nominal MRS optical train. The extra loss was identified (M. te Plate, ESA, private communication) as being caused by a fault in the groove profiles of the Channel 4 gratings which cannot be corrected before launch.

Following the procedure to determine the photon conversion efficiency, we can establish a first spectrophotometric calibration. By comparing the flux conversion factors derived from blackbody measurements of the MTS at 400, 600 and 800K, we can assess the achievable spectrophotometric calibration accuracy. Figure 22 shows the ratios of the different obtained flux conversion factors as a function of wavelength. We are encouraged by the good agreement (less than 2 % variation) over a large swathe of the MRS wave-band.

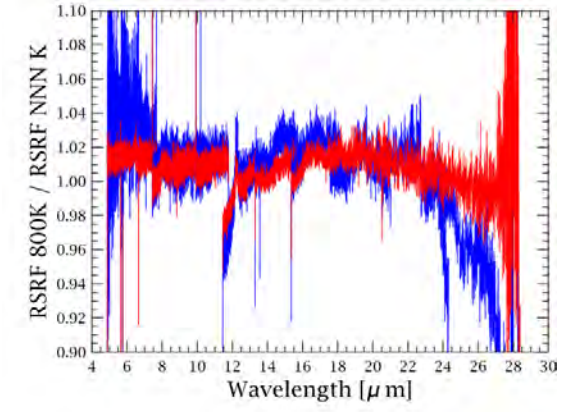

Figure 22. Comparison of the Relative Spectral Response function calculated using observations of the MTS black body at 400 K (blue) and at 600 K (red) with the RSRF at 800 K.

3.9 MRS Straylight

As described in Section 2.3 great care was taken to minimise sources of straylight and optical cross-talk within the MRS IFUs. However, a source of straylight was detected during RAL testing, which was identified as being caused by scattering in optical components within the SMO. The stray light is manifested as a signal that extends in the detector row direction. Its magnitude is proportional to that of bright illuminated regions of the spectral image, at a ratio that falls with increasing wavelength, from about 2 % in Channel 1A to undetectably low levels long-ward of Channel 2B.

Figure 23 emphasises the impact of the straylight in Channel 1B, using the wavelength averaged, reconstructed image of a bright source (seen at the top-left). The straylight signature is seen as the two horizontal bands, where the variation in brightness with the 'alpha' coordinate is well explained by the mapping between alpha and detector row coordinate.

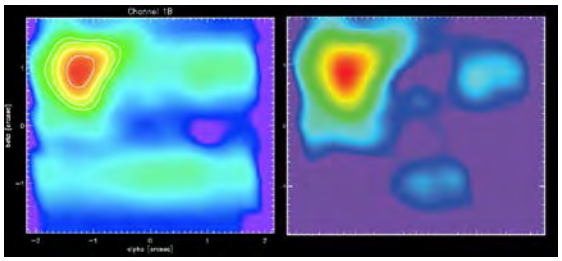

Figure 23. Straylight in Channel 1B. Left: The reconstructed image of a bright, moderately compact source is plotted on a logarithmic scale with contours at 50, 20, 10 and 5 % of the peak signal level. Right: The image after stray-light correction using a proto-type algorithm.

The development of algorithms for correction of this straylight is underway. They take advantage of the stray-light being the dominant signal in the inter-slice regions of the detector, thereby making it amenable to accurate characterisation. Initial indications (Figure 23) suggest that an effective correction algorithm will be available before launch.

3.10 Spectral Leakage

Testing at RAL revealed a gap in the performance of the train of dichroics described in Section 2.2. The set of filters that define the pass-band for Channel 3, Sub-band A have an unwanted (but small) transmission peak at a wavelength of 6.1 μm, which allows light in the second diffraction order to reach the detector at the position where 12.2 μm light is detected in the first diffraction order. This leak was confirmed using Fabry-Pérot etalon data and characterised to produce the leak profile plotted in Figure 24. This curve can be interpreted as the transmission profile by which a target object's 6.1 μm spectrum should be multiplied in order to determine the leakage signal at 12.2 μm.

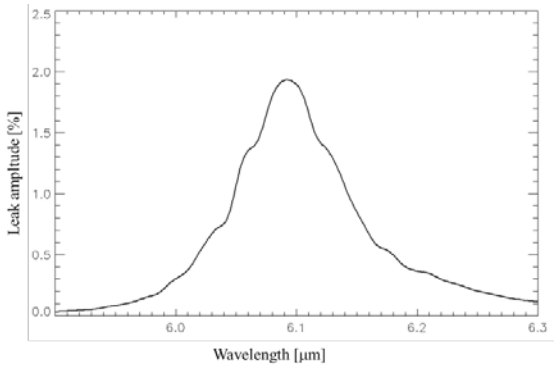

Figure 24. MRS Channel 3A spectral leak profile. This is the fraction of the source spectrum at λ = 6.1 μm which is added to the nominal 12.2 μm spectrum.

There are two options for mitigating the effects of the spectral leak. First, the Channel 3A spectrum can be corrected by multiplying an observation of the target object's 6.1 μm (Channel 1B) spectrum by the leak profile, resampling the wavelength scale of the resulting spectrum to the wavelength grid of Channel 3A and then subtracting it from the contaminated Channel 3A spectrum. This requires that a separate Channel 1B observation has been taken.

The second method would be to make the Channel 3A observation with Dichroic Wheel 1 set to use the Sub-band B dichroics (see Section 2.2 to see what this means in terms of the optical train). This combination of dichroics reduces the spectral leak by a factor of more than 1000 at λ = 6.1 μm. The unwanted side-effect of this solution is a loss of PCE at the short wavelength end of Channel 3A which would now fall from its nominal 0.12 el phot^{-1} at λ = 11.8 μm to only 0.02 el phot^{-1} at the short wavelength limit of λ = 11.47 μm.

4 CONCLUSION

We have presented the key parameters that describe the performance of the MIRI MRS spectrometer as designed or measured, in a form that both provides our best estimate of the instrument's behaviour on-orbit and also that is accessible to the prospective user. The optical design behind the parameters is presented at a level of detail that is intended to provide the astronomer with an understanding of what to expect in terms of operating restrictions and data format when planning observations.

The impact of straylight and spectral leaks in contaminating the spectral images has been discussed,

along with proposals of operational and analytical techniques that should mitigate their effects. When combined with the latest sensitivity estimates (Glasse et al., 2014, Paper IX), we are confident that the MIRI MRS will meet all of its scientific objectives as part of the JWST Observatory.

ACKNOWLEDGEMENTS

The work presented is the effort of the entire MIRI team and the enthusiasm within the MIRI partnership is a significant factor in its success. MIRI draws on the scientific and technical expertise of the following organisations:

Ames Research Center, USA; Airbus Defence and Space, UK; CEA-Irfu, Saclay, France; Centre Spatial de Liége, Belgium; Consejo Superior de Investigacones Científicas, Spain; Carl Zeiss Optronics, Germany; Chalmers University of Technology, Sweden; Danish Space Research Institute, Denmark; Dublin Institute for Advanced Studies, Ireland; European Space Agency, Netherlands; ETCA, Belgium; Goddard Space Flight Center, USA; Institute d'Astrophysique Spatiale, France; Instituto Nacional de Técnica Aerospacial, Spain; Institute of Astronomy, Zurich, Switzerland; Institute for Astronomy, Edinburgh, UK; Jet Propulsion Laboratory, USA; Laboratoire d'Astrophysique de Marseille (LAM), France; Lockheed Advanced Technology Center (USA); NOVA-Astron; Northrop Grumman, USA; Max-Planck Institut fqr Astronomie (MPIA), Heidelberg, Germany; Observatoire de Paris, France; Observatory of Geneva, Switzerland; Paul Scherrer Institut, Switzerland; Physikalishes Institut, Bern, Switzerland; Raytheon Vision Systems, USA; RUAG Aerospace, Switzerland; Rutherford Appleton Laboratory (RAL), UK; Space Telescope Science Institute, USA; Toegepast Natuurwetenschappelijk Onderzoek (TNO-TPD), Netherlands; UK Astronomy Technology Centre UK; University College London, UK; University of Amsterdam, Netherlands; University of Arizona, USA; University of Cardiff, UK; University of Cologne, Germany; University of Ghent; University of Groningen, Netherlands; University of Leicester, UK; University of Leiden, Netherlands; University of Leuven, Belgium; University of Stockholm, Sweden; Utah State Univ., USA;

We would like to thank the following National and International Funding Agencies for their support of the MIRI development :

NASA, ESA, Belgian Science Policy Office, Centre Nationale D'Etudes Spatiales, Danish National Space Centre, Deutsches Zentrum für Luft- und Raumfahrt (DLR), Enterprise Ireland, Ministerio De Education y Ciencia, NOVA, Science and Technology Facilities Council, Swiss Space Office, Swedish National Space Board, UK Space Agency

REFERENCES

Browder, J.S., Ballard, S.S., 1969, Appl. Optics, Vol.8, No.4, 793B.

Browder, J.S., Ballard, S.S., 1972, Appl. Optics, Vol.11, No.4, 841B.

Fruchter, A. S., Hook, R. N., 2002, PASP, 114, 144F

Glasse., A.C.H., et al., 2014, PASP, **Paper IX**

Glasse, A. Lee, D., Parr-Burman, P., Hayton, D., Mazy, E., 2006, SPIE, 6265, p 118.

Glauser, A. M., Glasse, A. C. H., Morrison, J. E., Kelly, B. D., Wells, M., Lahuis, F., Wright, G., 2010, SPIE, 7731, 77313K.

Hawkins, G. J., Sherwood, R. E., Barrett, B. M., 2007, Proc. OSA Technical Digest Optical Interference Coatings, WDPDP1, ISBN: 1-55752-841-1

Kester, D. J. M., Beintema, D. A., Lutz, D., 2003, proc. 'The calibration legacy of the ISO Mission', Eds. Metcalfe, L., Salama, A., Peschke, S. B., Kessler, M. F., ESA SP-481, p 375.

Lahuis, F., Boogert, A., 2003, proc. 'Chemistry as a Diagnostic of Star Formation', Eds. Curry, C.L, Fich, M., p 335.

Lahuis, F., van Dishoeck, E. F., 2000, A&A, Vol. 355, p 699.

Ramsay-Howat, S.K, Todd, S., Wells, M., Hastings, 2006, P., New Astronomy Reviews, Volume 50, Issue 4-5, p 351.

Rieke, G., et al., 2014, PASP, **Paper VII**

Ressler, M.E., 2014, PASP, **Paper VIII**

Smith, T.F., White, G.K., 1975, J. Phys. C: Solid state Phys. Vol.8, p.2031.

Wells, M., Hawkins, G. J., Olofsson, G, 2004, Optical, Infrared, and Millimeter Space Telescopes. Ed. Mather, J. C., Proceedings of the SPIE, Volume 5487, p 794.

Woods, S. I., Kaplan, S. G., Jung, T. M., Carter, A. C., 2011, Applied Optics, Vol. 50, Issue 24, p 4824.

Wright, G., et al., 2014, PASP, **Paper II**